Development of an Analysis and Optimization Tool for Slotted Wing Natural-Laminar-Flow Aircraft

Dimitri J. Mavriplis *, Zhi Yang † and Evan M. Anderson
Department of Mechanical Engineering, University of Wyoming, Laramie, WY 82071

A set of computational tools for aeroelastic analysis and optimization are validated and utilized for the goal of optimizing a slotted natural-laminar-flow (SNLF) wing design for commercial aircraft. The SNLF design has been shown to have enhanced lift/drag characteristics, with the potential to significantly reduce fuel burn at cruise conditions. The aeroelastic modeling capability combines a Reynolds-averaged Navier Stokes flow solver with a finite element modeling and optimization package for tightly coupled analysis. Both modeling packages feature the capability to obtain sensitivities of aerodynamic and structural objectives using the adjoint method for gradient-based optimization. A series of validation test cases are described and performed for the individual codes and coupled framework, and a design optimization study is performed for a notional SNLF aircraft configuration.

I. Introduction

The next generation of aerodynamic design faces the continuing challenge of reducing greenhouse gas emissions by seeking designs that enhance efficiency and minimize fuel consumption. Commercial aircraft are the primary target for such improvements, as they represent the largest portion of fuel consumption in aviation. One approach to reducing fuel consumption is through the implementation of a slotted natural-laminar-flow (SNLF)[1–5] wing design. In this design, the wing's cross section is composed of two separate elements, one fore and one aft, in such a way as to achieve predominantly laminar flow over the main element, and consequently reduce drag.

The present work is part of a collaborative investigation to reduce fuel burn of commercial aircraft by 70% compared to the 2005 baseline through theoretical developments, material selection and high-fidelity multi-disciplinary simulation and optimization under a NASA sponsored University Leadership Initiative (ULI) led by the University of Tennessee at Knoxville. The specific focus of this article is on the development and validation of a set of high-fidelity computational tools for analysis and optimization of flexible structures using gradient-based methods and applying these tools to the optimization of an SNLF wing.

In this work, the general aerodynamic analysis approach is based on a Reynolds-averaged Navier-Stokes (RANS) CFD methodology, using unstructured meshes in order to facilitate the use of complex geometries. RANS CFD methods currently constitute the high-fidelity analysis methodology of choice for industrial aircraft design and have been demonstrated to be very successful at predicting aerodynamic performance metrics including force and moment coefficients, particularly at the cruise condition, as evidenced by the conclusions of the AIAA Drag Prediction Workshop series.[6] However, in order to successfully predict the performance of an SNLF wing or SNLF wing-based

*Professor, AIAA Associate Fellow; email: mavriplis@uwyo.edu
†Research Scientist, AIAA member; email: zyang@uwyo.edu

aircraft, the analysis capability must incorporate various other disciplines which play a critical role in the design and ultimate performance of these configurations. Foremost, a natural transition prediction capability must be incorporated into the RANS methodology. Additionally, the sensitivity of the onset of transition to in-flight geometry, coupled with the use of highly flexible structures, results in the need to include the effect of the coupled aero-structural deflections in the analysis approach. Finally, in order to construct a successful optimization tool for SNLF configurations, an adjoint methodology which includes natural transition and aerostructural effects must also be devised and used to drive a gradient-based optimization strategy.

In this paper, we outline the development of an analysis and corresponding adjoint-based optimization tool for SNLF configurations. In addition to the base unstructured mesh CFD RANS analysis tool, three different partial-differential equation (PDE)-based natural transition models have been implemented and tested. An in-house structural modeling capability has also been developed which is tightly coupled with the RANS CFD analysis tool through a fluid-structure interface. The discrete adjoint of these individual disciplinary analysis solvers has also been implemented, enabling the computation of sensitivities for natural laminar flow aerostructural problems for use in design optimization studies.

In the following section of this paper, we discuss the rationale for and construction of a notional SNLF transonic truss-braced wing (TTBW) aircraft geometry used for demonstrating the tools developed in this work. In Section III, we outline the various individual disciplinary computational tools which have been developed for SNLF configurations. In section IV, we report on validation efforts for the natural transition analysis capability within the RANS CFD code, as well as validation of the aero-structural analysis capability. In section V, the developed computational approach is applied to the analysis of a notional SNLF TTBW configuration, and the demonstration of a design optimization of this configuration is discussed in Section VI. Section VII closes with a summary of current results and prospects for future work.

II. Slotted Natural Laminar Flow Transonic Truss-Braced Wing

In order to demonstrate the performance of the analysis and optimization tools developed in this work, a notional Slotted-Natural Laminar Flow Transonic Truss-Braced Wing (SNLF TTBW) configuration has been developed. The construction of this geometry relies on two distinct technologies, namely the SNLF airfoil technology developed in particular in reference,[3,7] and the TTBW concept studied extensively by NASA and Boeing.[8] The cross section of the SNLF wing is based on the S204 two-element airfoil developed by Airfoils Inc. and discussed in reference.[3] For this configuration, flow over the larger main element is mostly laminar, and the majority of the lift is produced by the aft element.

The planform for this SNLF wing is loosely based on the SUGAR-High or 765-095 configuration developed by Boeing and detailed in reference.[8] Our wing has an aspect ratio of 22, a quarter chord sweep of 8°, a taper ratio of 0.346, and zero dihedral. This wing was mated to a fuselage and empennage provided by Boeing and based on the geometry developed in reference.[8] A rounded wing tip along with fairings at the fuselage-wing intersection were designed by hand in SolidWorks. The complete geometry is depicted in Figure 1. An unstructured mesh for aerodynamic CFD analysis about this configuration was constructed using the Pointwise software. The mesh contains a total of approximately 9 million grid points, with tetrahedral elements in outer flow regions and prismatic elements in boundary layer regions with a wall normal spacing of 10^{-6} based on the mean aerodynamic chord. After subsequent CFD analyses, the fuselage-wing fairing was found to be poorly designed, resulting in some amount of flow separation at the cruise condition. This anomaly contributes to higher than expected overall drag in the reported analyses in this paper. However, due to the notional nature of this configuration, it was decided to proceed with the current

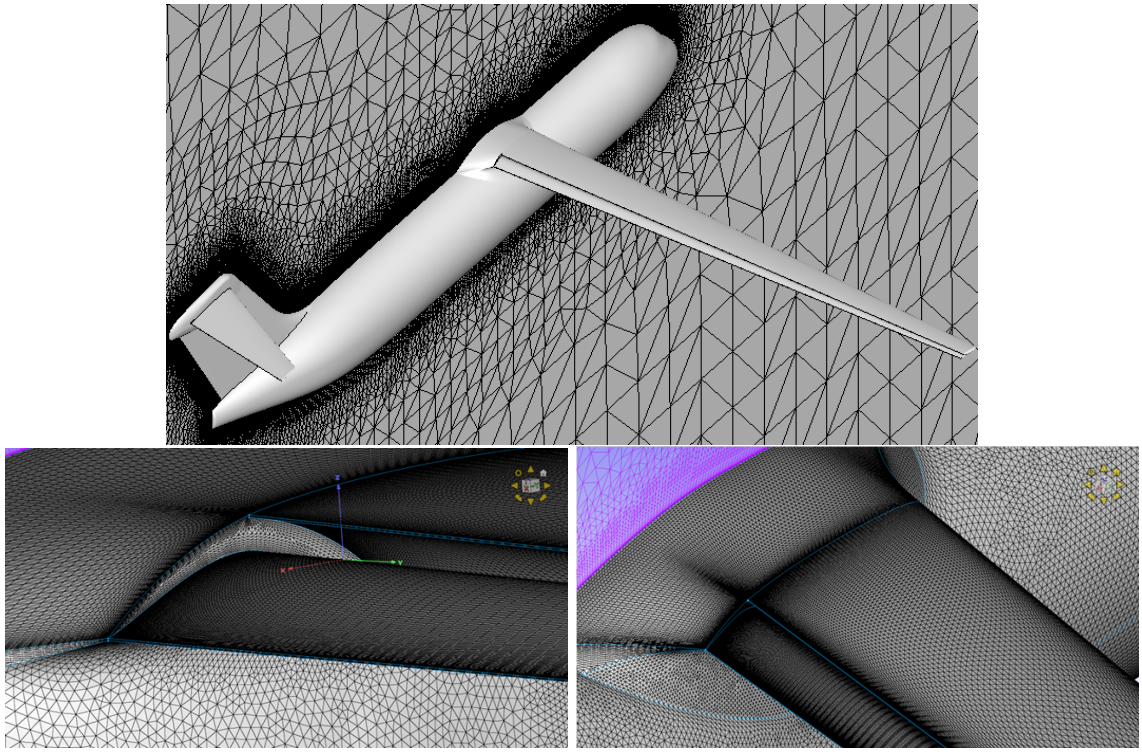

Figure 1. Illustration of SNLF aircraft geometry and associated unstructured mesh for CFD analysis

.

geometry for the purposes of demonstrating the developed computational tools. A more refined configuration is currently under development in collaboration with Boeing and other members of the NASA ULI project supporting this work. A wing strut was also designed, and attached to the wing and fuselage at the same locations as detailed in reference.[8] However, the design of suitable fairings at these intersections also proved problematic. Therefore, for current purposes, the strut was not included in the aerodynamic configuration, although it is present in the structural model.

A matching structural model was developed for the wing box and strut of the aerodynamic configuration discussed above. This model was developed using the ABAQUS commercial software, which outputs model files that are compatible with our in-house developed structural model. The wing box structural model consists of an upper panel, a lower panel, a leading edge spar and a trailing edge spar, and is divided into 48 equally spaced spanwise sections joined by ribs running in the chord direction. All wing sections are constructed of 4-node shell elements. A coarse-meshed model was constructed with a total of 17,300 elements, along with a fine-meshed version containing 69,200 elements. The wing box cross section runs from 10% chord to 60% chord, conforming to the outer mold line of the fore element of the digitized S204 airfoil. The strut of the wing is modeled with a series of 2-node beam elements connected to the mid-span section of the lower panel, running to the point 4.5 meters below the wing level at the aircraft centerline, in accordance with the fuselage design furnished by Boeing. The current model is defined with all aluminum construction, with panel thicknesses set to approximately match the cross-sectional stiffness data provided for the SUGAR-High configuration.[8] The structural analysis is performed with both the root of the wing and the fuselage-anchored end of the strut fixed to zero displacement and rotation to simulate a symmetric aircraft condition. An illustration of the structural model is provided in Figure 2.

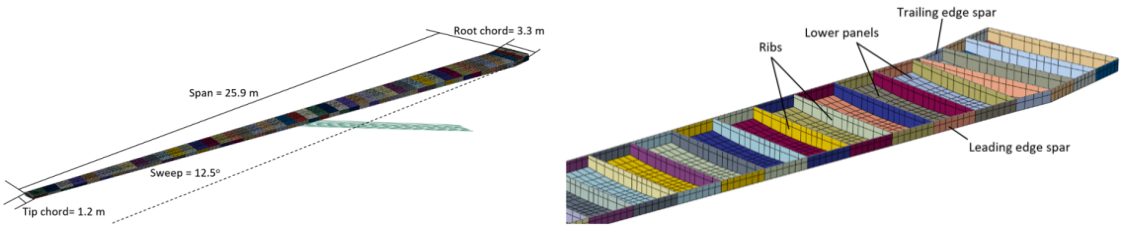

Figure 2. Illustration of structural wing-box and strut model for SNLF wing geometry

.

III. Methodology

Reynolds-Averaged Navier-Stokes Solver: The aerodynamic analysis capability for this work is based on the NSU3D unstructured mesh RANS CFD solver.[9] NSU3D operates on hybrid meshes using prismatic elements in boundary layer regions and tetrahedral meshes in outer regions with small numbers of pyramidal elements occurring at the edge of boundary layer regions. The employed discretization is based on a finite-volume approach with matrix-based artificial dissipation which is nominally second-order accurate. The current work makes use of the Spalart-Allmaras (SA) turbulence model which follows the implementation devised for avoiding negative eddy viscosity values, described in reference.[10] The basic solver employs a line-implicit method, which is used as a smoother on fine and coarse levels of an agglomeration multigrid solver.[11] This basic solver strategy can be employed directly as an iterative nonlinear solver, or as a linear preconditioner for use in a Newton-Krylov method. NSU3D has been well validated for low-speed and transonic cruise problems as a regular participant in the AIAA High Lift Prediction Workshop (HLPW) series[12] and the Drag Prediction Workshop (DPW) series.[13] NSU3D also includes an exact discrete adjoint capability, which has been verified to machine precision compared to the complex step and forward sensitivity methods using the SA turbulence model.[14] The adjoint problem is typically solved using an analogous restarted GMRES approach with a line-implicit multigrid preconditioner.

Transition Modeling: One of the major efforts of the current work has been the implementation and testing of various PDE-based transition models for predicting natural laminar flow transition to turbulence. To date, three different models have been implemented including the Langtry-Mentor model,[15] the Coder AFT2 model,[16] and the single equation γ model of Mentor.[17,18] One of the deficiencies of the implemented models is that they do not account for spanwise flow induced transition effects. However, due to the high-aspect ratio and low sweep of the current configuration, this may be an acceptable compromise, although the implementation of additional cross-flow correlation terms is planned for the future. These models are solved in a tightly coupled fashion with the corresponding turbulence modeling and flow field equations. For example, using the two-equation AFT2 model with the k-omega or SST two-equation turbulence model results in block 9x9 matrices where the individual blocks are inverted directly. For the design optimization capability, the exact discrete adjoint of the fully coupled system of transition-turbulence-flow equations has also been implemented and verified. This adjoint system is solved using a restarted GMRES approach with a line-implicit multigrid preconditioner. Accurate sensitivity calculation using the adjoint method relies on the availability of a well converged primal (i.e. analysis) problem, which determines the flow state about which the sensitivity equations are linearized. Additionally, it is well known that the corresponding adjoint system becomes more difficult or even impossible to solve if the primal state is poorly converged. One of the difficulties encountered with the transition model implementation

is the ability to fully converge the coupled transition-turbulence-flow equations to machine zero or at least to very low steady-state residual levels. For these reasons, we have focused on the use of the single equation transition model of Mentor[17,18] coupled to the Spaart-Allmaras turbulence model for use in the design optimization tool. Convergence with this model has been found to be more robust than with the models involving larger numbers of equations. However even with this approach, stalled convergence is often observed. The mechanism has been traced back to isolated points in the laminar sublayer regions, downstream of the transition region, where the intermittency values in the transition equation jump between small and large values. In all cases observed to date, these regions are far removed from the transition location and do not significantly influence the overall transition results. Therefore, after an initial phase of convergence, the intermittency values are frozen in the transition model. This has been found to enable convergence to machine precision and thus facilitate the solution of the adjoin system for the required sensitivities.

Structural Modeling: The in-house developed code AStrO,[19,20] is used to predict structural deflections in response to aerodynamic loading. AStrO is a finite-element based structural code which implements a subset of the common brick and shell element types encountered in commercial structural analysis codes. AStrO supports standard tri-linear 8-node brick elements, as well as the corresponding degenerate 6-node wedge (pyramidal) and 4-node tetrahedral elements. Additionally, 8-node incompatible mode elements have been implemented. These element types show significant improvement in accuracy as compared to the original tri-linear formulation, particularly for problems with high bending loads, but remain substantially less computationally expensive compared to the quadratic 20 node hexahedral elements. In addition, two types of shell elements have also been implemented: 3-node triangular shell elements and 4-node quadrilateral shell elements. The governing equations for the structural response are derived from the widely used virtual work formulation. AStrO supports geometrically nonlinear structural problems, although only linear elasticity has been used in the current work. A design feature of the in-house FEM structural analysis code is that it should be compatible with existing commercial structural analysis software tools such as Abaqus and Nastran. Therefore, the in-house structural solver contains an interface that can directly read in model files generated within Abaqus.[19] Structural models built using other commercial tools such as Nastran can be read into Abaqus and translated to the Abaqus file format, which in turn can be read in by AStrO. The implementations of the various supported element types have been verified by performing unit tests on each element type and comparing with analytic solutions when available, and with the equivalent solutions generated by Abaqus. Validation experiments have also been performed on various simple structural models with mixtures of the supported elements by comparing computed stress, strain and deflection results with those produced by Abaqus. The structural equations are solved directly using Cholesky sparse matrix factorization. To optimize performance, an algorithm to rearrange the global node-ordering and minimize the bandwidth of the linear system is implemented, following the basic algorithm of Sloan.[21] The general software framework allows for multiple structural models to be run on different processors or cores, for example in the case of four blades of a helicopter rotor. However each individual model must be run on a single core. The use of parallel direct solvers such as MUMPS[22] has been investigated but is not employed in the current work.

Fluid-Structure Interface: In order to couple the computational structural dynamics (CSD) solver to the computational fluid dynamics (CFD) solver, a general fluid-structure interface (FSI) module has been developed. This interface is a stand-alone module that transfers the aerodynamic forces from the computational fluid dynamics (CFD) solver to the computational structural dynamics (CSD) model, and also returns the displacements generated from the CSD solver to the CFD surface mesh. The FSI must be capable of handling non-point matched overlapping CFD and CSD surface meshes of widely varying resolution and element types. Additionally, the FSI must be

capable of handling CSD models that do not match the outer-mold line (OML) of the geometry used for the CFD surface mesh. This situation can arise either due to small differences in the geometry representation used for the CFD and CSD model, or due to an incomplete CSD model, for example in cases where only a portion of the complete structure is used in the CSD model, as is often the case in early design stages. In order to accommodate these different cases, the FSI represents the CFD surface mesh as a cloud of points, which enables a unified approach for structured and unstructured surface meshes. For each CFD surface point, the closest point on the surface of the CSD finite element mesh is found through a fast parallel search technique, which is based on the minimum distance search used for CFD turbulence model requirements. Once all CFD surface points have been associated with their closest perpendicular projection on the CSD surface mesh, the CFD forces are transferred to the CSD surface nodes as:

$$F_{CSD} = [T]F_{CFD} \tag{1}$$

where [T] represents the rectangular transfer matrix which is computed assuming the surface CFD points are attached to their corresponding closest point on the surface CSD mesh via rigid links. Conversely, the CSD displacements are transferred back to the CFD surface mesh as:

$$U_{CFD} = [T]^T F_{CSD} \tag{2}$$

By using the transpose of the force transfer matrix for the displacement transfer, the principle of conservation of virtual work is satisfied. To enhance robustness and increase flexibility, all CFD surface points and CSD surface faces are associated with a component number and the user can specify which CFD components should transfer forces to which CSD components. In this manner, specific components that do not contribute to loads on the flexible structure can be omitted.

Geometry Modeling: A facility for parametrizing and modifying the geometry is required for design optimization problems. The adopted strategy is aimed at working with familiar wing design parameters typically employed in a lofting process. The geometry modeling code allows for a prescribed number of airfoil defining cross-sections. Each airfoil is itself parametrized using either Hicks-Henne bump functions or using the class function / shape function transformation technique (i.e. CST functions), which may include thickness constraints.[23] The airfoils are then stacked in the spanwise direction and a planform is defined based on the sweep angle and taper ratio. Additional design variables can be defined such as thickness ratios, spanwise twist, and dihedral/anhedral. Once all the input shape design parameters are specified, a three-dimensional wing geometry is created and output as a single block structured surface mesh of prescribed resolution. This constitutes the baseline or nominal geometry model, which can then be translated and/or rotated to line up or coincide with the actual wing geometry in the CFD and CSD model reference frames. Additionally, a single geometry component may be used for multiple corresponding component instances in the CFD/CSD models, such as left and right wing sections or flaps. As the design optimization calculation progresses and new shape changes are induced by variations in the design parameters, the changes between the new shape and the nominal geometry model are computed and interpolated onto the CFD and CSD surface meshes. This is achieved using the same closest point search to associate the CFD/CSD surface mesh points to their closest normal projection point on the geometry model. The search is performed once for the nominal configuration, and the CFD/CSD surface meshes are then assumed to be linked to the geometry model by rigid links that move with the design changes applied to the geometry model. Similarly to the fluid-structure interface described above, this approach allows for nonconforming or inexact fits between the nominal geometry model and the corresponding CFD/CSD surface meshes.

Mesh Deformation: A mesh deformation capability is required in order to deform the unstructured CFD volume mesh in response to surface mesh displacements which occur throughout the simulation process. For aero-structural problems, these surface displacements occur as a result of the surface deflections computed by the structural model in response to CFD computed aerodynamic loads, which are transferred back to the CFD surface mesh through the FSI. Additionally, for shape optimization problems, design changes of the aerodynamic outer mold line must also be propagated into the interior CFD mesh. The mesh deformation approach adopted in this work is based on a linear elastic analogy whereby the unstructured CFD mesh is modeled as a linear elastic solid which deforms in response to prescribed surface deflections.[24] The modulus of elasticity of the

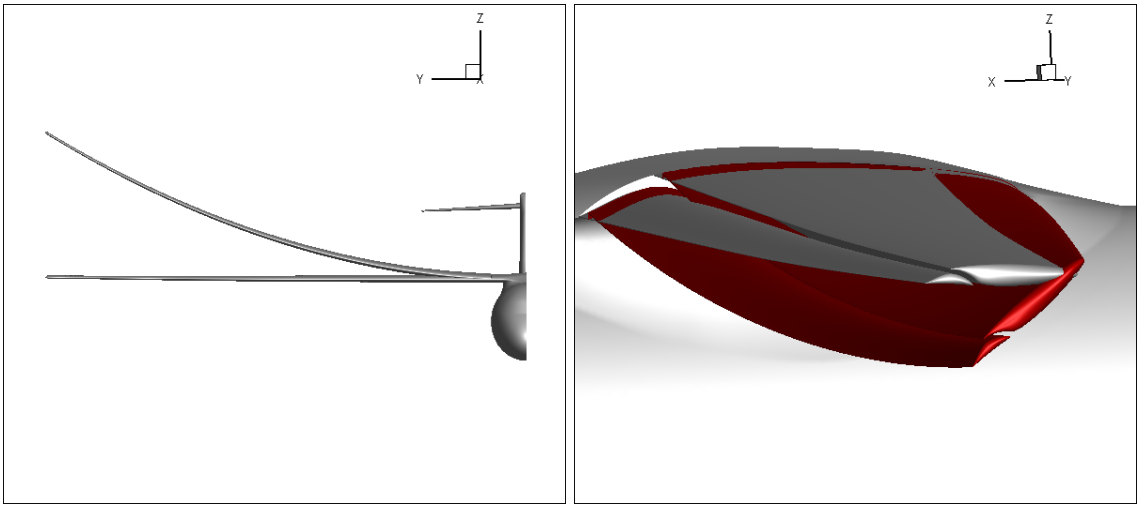

Figure 3. Illustration of limits of linear elastic mesh deformation in bending (left) and twist (right) prior to the development of invalid negative cell volumes for SNLF geometry

.

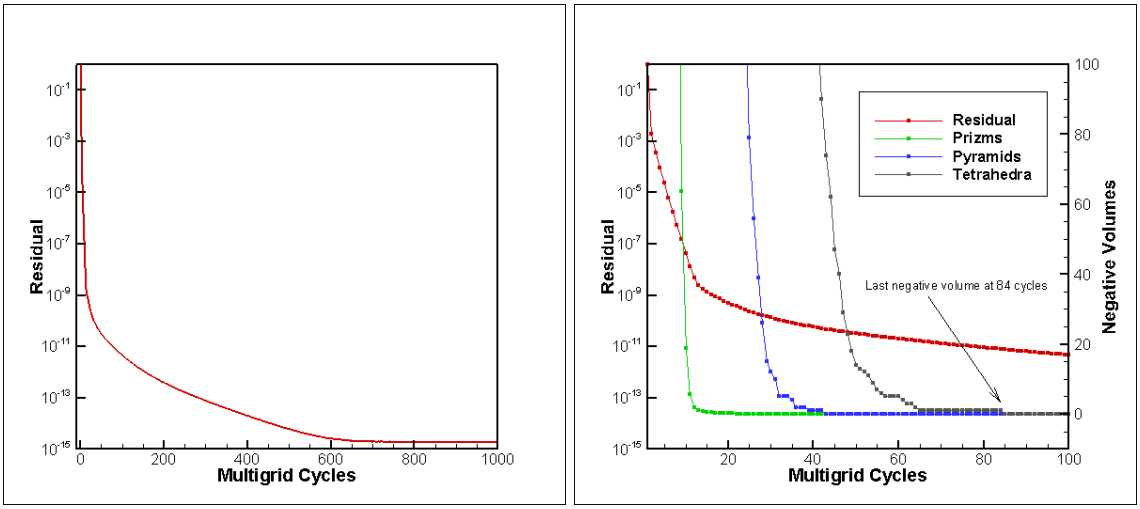

Figure 4. Convergence of mesh deformation solver for maximum wing bending test case shown above in term of multigrid cycles and in terms of number of negative cell volumes.

.

mesh elements can be set either as inversely proportional to the cell volume, or as a function of the distance from the deflecting surface. In both cases, this results in stiff elements near the surface and more compliant elements away from the surface, thus preserving element shapes and avoiding negative volumes in regions near the deflecting surface. The mesh deformation equations are discretized using a second-order accurate continuous Galerkin finite-element approach, and the resulting equations are solved using the same parallel line-implicit multigrid algorithm employed for the flow solver. Figure 3 illustrates the robustness of this approach by showing the limits in wing bending and twisting that can be accommodated without developing negative volume (invalid) cells for the mesh generated about the SNLF configuration. The mesh deformation equations converge monotonically to machine zero using the multigrid algorithm in approximately 600 cycles as shown in Figure 4, with the number of invalid cells being eliminated usually in less than 100 multigrid cycles.

IV. Validation Test Cases

In this section we present three validation test cases. The first two cases provide validation of the natural laminar flow transition models for airfoil and wing configurations, while the third test case focuses on validation of the aero-structural analysis capability for fully turbulent flows in the absence of a transition model.

A. S204, slotted Natural-Laminar-Flow Airfoil

Since our notional SNLF wing geometry is based on the S204 airfoil, an appropriate first validation test case consists of the computation of the free transition flow over the S204 airfoil in two dimensions over its range of design operating conditions. The S204 is a two-element configuration designed to achieve higher lift coefficients and lower drag coefficients than single-element natural-laminar-flow airfoils. The S204 airfoil is designed in such a way to keep the fore element entirely laminar in order to reduce overall drag. The SNLF concept as well as the S204 configuration is proprietary to Airfoils Inc. and protected by a patent, requiring a license for its use. The specific airfoil geometry used in this paper was obtained by digitizing a figure of the airfoil geometry in reference[3] with permission from the author. Because the performance of SNLF airfoils can be sensitive to small geometry perturbations, this approach may not be entirely accurate due to the approximate airfoil coordinates used in this case. Figure 5 shows the near field mesh for the S204 airfoil. The normal wall spacing in this mesh is 1.2×10^{-6} chord lengths. There are 390 surface mesh points on the main element and 226 points on the flap. The total number of mesh points is approximately 51,000. The flow is computed using the NSU2D unstructured mesh CFD code, which is the two-dimensional counterpart to the NSU3D CFD code used subsequently for three dimensional configurations. The computed drag polars for $Mach = 0.5$, $Re = 12 \times 10^6$ and freestream turbulence intensity $Tu = 0.07\%$ are plotted in Figure 6. The agreement between the transitional predictions and the reference results[3] is generally good. Figure 7(a) shows the pressure coefficient distribution at $\alpha = 0^\circ$. The skin-friction distribution at $\alpha = 0^\circ$ is shown in Figure 7(b), which shows entirely laminar flow on the fore element upper surface.

B. TU Braunschweig Sickle Wing

The TU Braunschweig sickle wing transition experiment conducted by Petzold and Radespiel[25] provides a three-dimensional benchmark case for transition prediction. The wing geometry consists of a constant airfoil cross section and four spanwise sections with constant sweep angle for each section. The sweep angle for each section increases outboard, from 0° at the root section, to 30° at the 2nd section, 45° at the 3rd section and 55° at the tip section. The simulation conditions

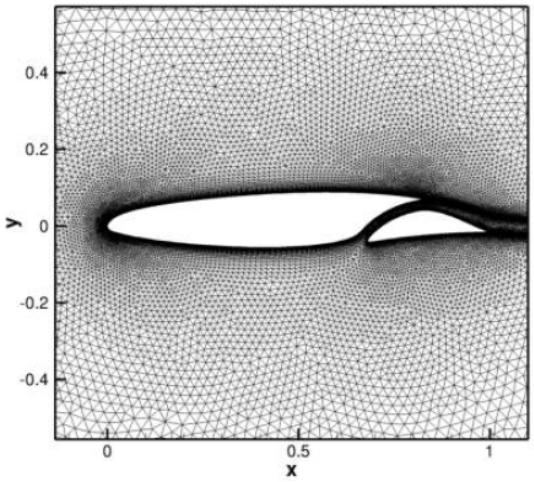

Figure 5. Two-dimensional unstructured mesh used for S204 airfoil calculations

.

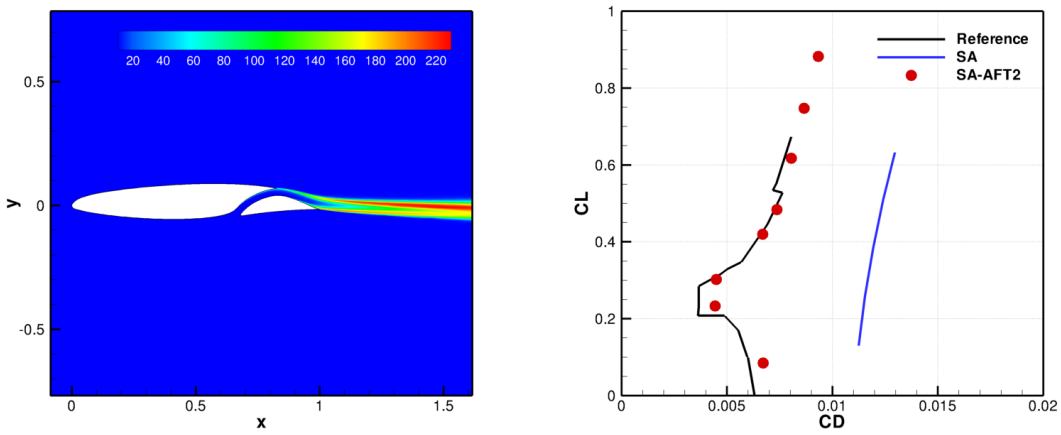

Figure 6. Eddy viscosity contours(left) and computed drag polar comparison with experiment from reference[3](right) at $Mach = 0.5$, $Re = 12 \times 10^6$ and $Tu_\infty = 0.07\%$ for the S204 slotted airfoil

.

for this geometry are $Ma = 0.156$, $Re = 2.7 \times 10^6$ and angle of attack $\alpha = -2.6°$. The freestream eddy viscosity ratio was set to 0.1 for the single equation Mentor results and the freestream turbulence intensity $Tu = 0.09\%$ was used for the AFT2 results. The computational grid consists of an unstructured mesh with approximately 7 million grid points with prismatic elements in boundary layer regions and tetrahedral and hexahedral elements elsewhere, as illustrated in Figure 8. The wall normal spacing is specified as 10^{-6} chords over the wing surface. The computational results are shown in Figure 9 and 10 in terms of computed skin friction distributions on the upper and lower surface of the wing, where they are compared with transition prediction results from reference[26] using the Coder AFT2-2019 model. The current computations include results using both the Coder AFT2-2019 model and Menter's one equation model. In all cases these models are coupled to the Spalart-Allmaras turbulence model. The general agreement between these two model implemen-

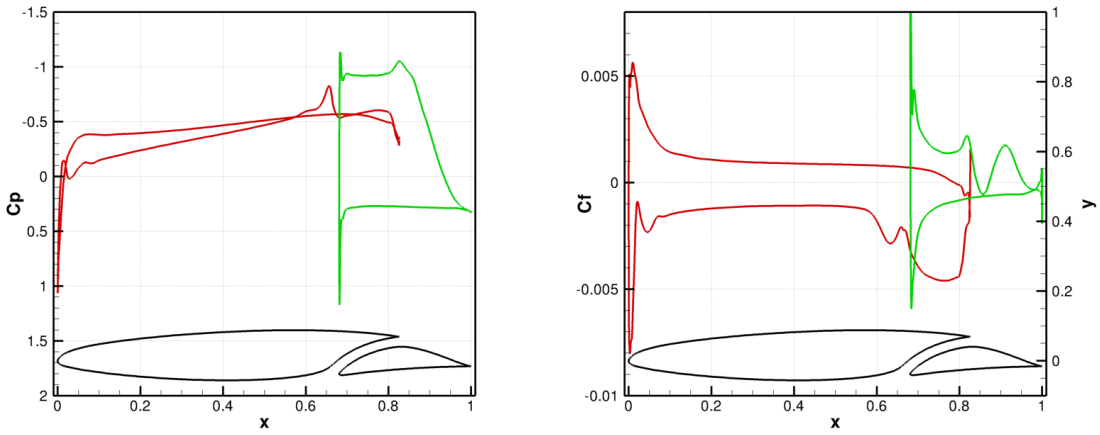

Figure 7. Pressure distributions(left) and the skin-friction distributions(right) at $M = 0.5$, $Re = 12 \times 10^6$ and $Tu_\infty = 0.07\%$, $\alpha = 0^\circ$ of the S204 slotted airfoil

.

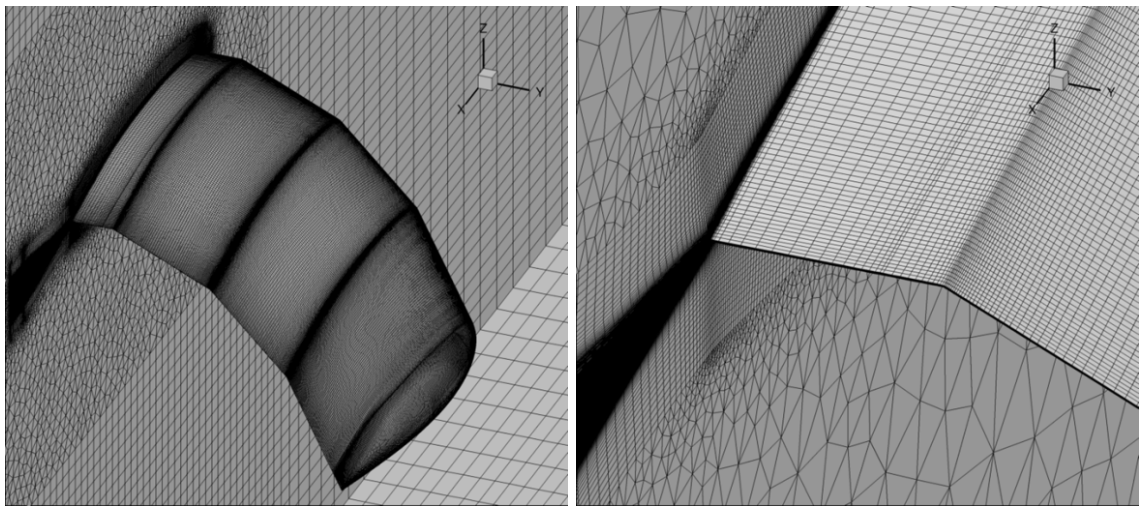

Figure 8. Illustration of unstructured mesh used for transitional flow over sickle wing geometry.

.

tations in the current work is good, and compare favorably with the predicted transition results from reference[26] using the AFT2-2019 model. For the lower surface, the computed results and the predictions from reference[26] compare well with the experimental results from reference.[25] On the upper surface the transition is known to be induced by cross flow instabilities. As expected, the results obtained using these two models do not agree well with experiment since these models do not account for cross flow instabilities. However, the agreement between the results obtained with the two models implemented in this work, as well as the agreement with the results presented in reference,[26] provide a level of verification that the models are implemented and solved correctly.

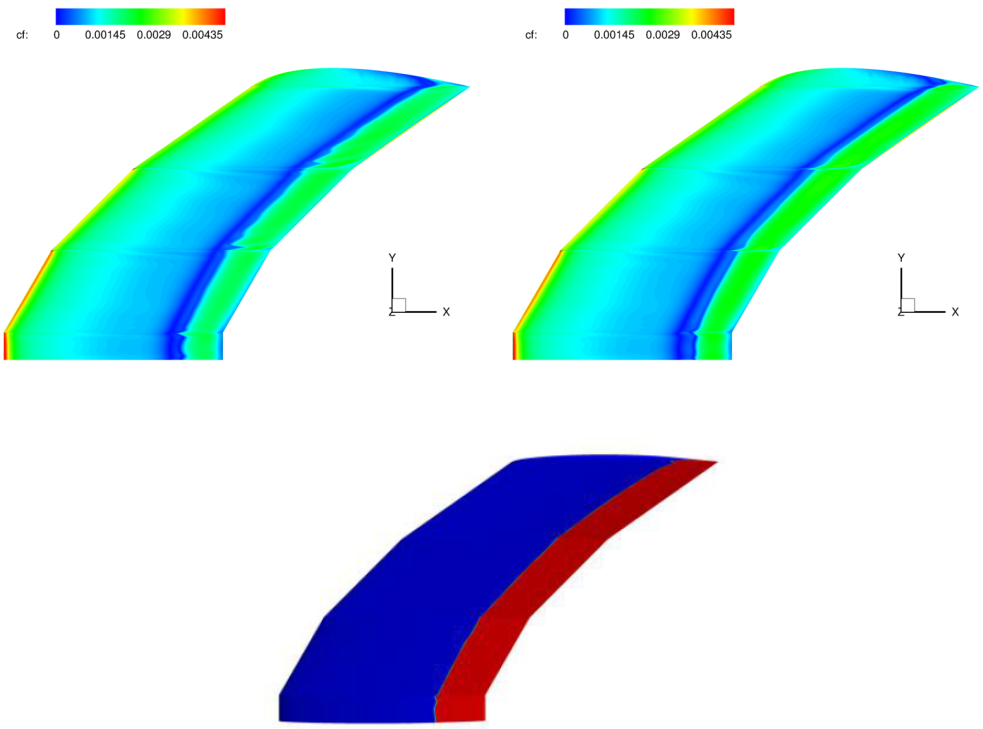

Figure 9. Comparison of transition locations as determined by skin friction distribution from current calculations using CoderAFT2-2019 model (top left), Mentor one equation model (top right) compared with transition location computed using Coder AFT2-2019 model from reference[26] for upper surface.

.

C. Undeflected CRM Aerostructural Validation Model

In reference,[27] Brooks et al. define a benchmark aerostructural model based on the NASA Common Research Model (CRM). The original CRM consists of a wing body with a 1g deflection built into the wing geometry, intended for aerodynamic analysis about the cruise condition. Due to this predefined deflection, the original CRM geometry is not suitable for aeroelastic analysis and optimization studies. In reference,[27] a notional wing box structural model is constructed, and the undeflected shape of the CRM wing is reverse engineered using an aerostructural optimization strategy. Taken together, the published undeflected CRM geometry, along with the provided structural model, constitute a suitable benchmark aerostructural validation test case, which should recover the 1g shape and aerodynamic performance of the original CRM at the nominal cruise condition. The published benchmark test case includes a sequence of coarse, medium and fine meshes for both the structural model and the CFD model. In this work we make use of the provided coarse resolution structural model, but employ our own CFD unstructured mesh generated about the published undeflected CRM geometry denoted as uCRM9.[27]

The structural model consists of a wingbox structure with upper and lower skins, as well as internal ribs and spars all constructed with blade-stiffened panels. A collection of lumped masses are distributed throughout the structure to simulate the effect of the engine, fuel and mounted actuators along the leading and trailing edges. For all studies discussed herein the wing material is aluminum 7000 series alloy. In the finite element model all sections are composed of 4-node shell elements. For simplicity and computational efficiency, the model does not include the panel stiffeners in the geometry/mesh definition. Brooks et al.[27] account for the effect of the stiffeners

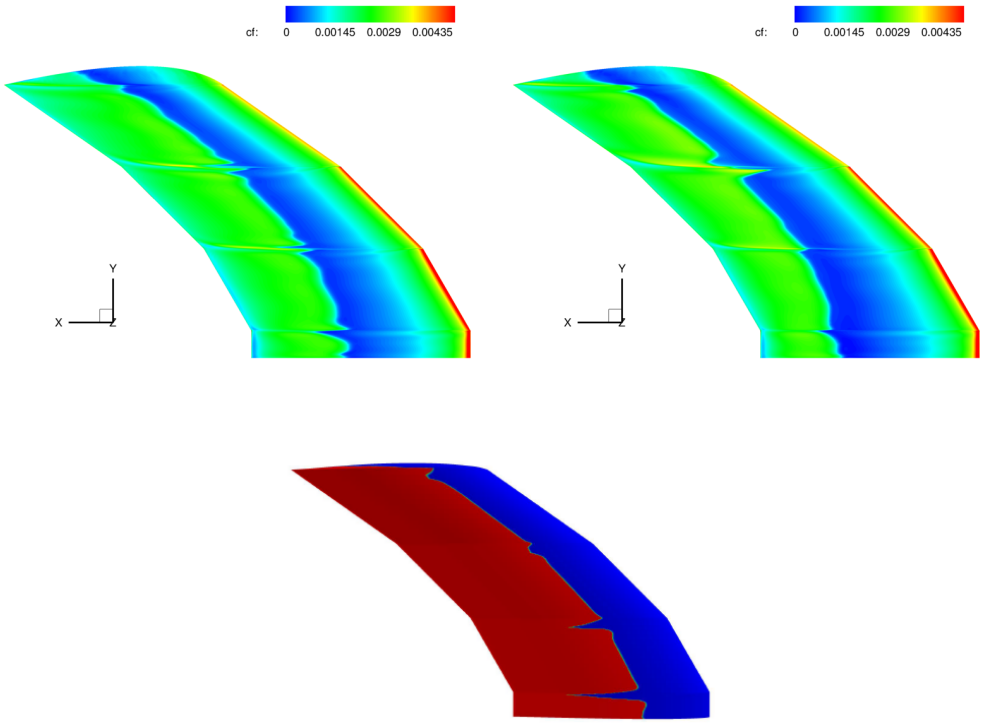

Figure 10. Comparison of transition locations as determined by skin friction distribution from current calculations using CoderAFT2-2019 model (top left), Mentor one equation model (top right) compared with transition location computed using Coder AFT2-2019 model from reference[26] for lower surface.

.

by incorporating them into the overall shell stiffness properties of each panel following the work of Kennedy et al.,[28] thus creating a homogenized panel with behavior equivalent to that produced by the presence of the stiffeners. The present work uses a different yet similar approach to modeling the panel stiffeners. A panel with stiffeners of a given width, height and spacing can be modeled as a two-layer composite laminate, with one layer representing the panel and the other representing the stiffeners. By defining the stiffeners as a second distinct layer, the dimensions and spacing of the stiffeners can be set directly as design variables in a way that is convenient and amenable to the input format of the structural solver while preserving the same effective panel stiffness.

An unstructured mesh of approximately 1 million grid points has been generated about the uCRM9 configuration and is used in the place of the structured CFD meshes provided in the benchmark test case.[27] The unstructured mesh contains tetrahedral elements in inviscid flow regions and predominantly prismatic elements in boundary layer regions, with a normal wall spacing of approximately 10^{-6} based on the mean aerodynamic chord along the wing. This unstructured mesh corresponds roughly to the resolution of the coarse structured CFD mesh provided in reference.[27] The structural model and CFD mesh in the vicinity of the wing are depicted in Figure 11.

In the current work, the Spalart-Allmaras turbulence model is used and the flow is assumed to be fully turbulent, which is consistent with the approach employed by Brooks et al.[27] in the definition of this test case. The coupled aero-structural problem is solved at the nominal cruise condition ($Ma = 0.85$, $C_L = 0.5$, Altitude = 37,000 ft). However, rather than using a fixed C_L condition, a fixed angle of attack of 2 degrees was used, which corresponds closely to the final flow incidence of 2.014 degrees obtained in the original study.[27] Figure 11 illustrates the solution obtained at these conditions both in terms of the computed surface pressure coefficient and the

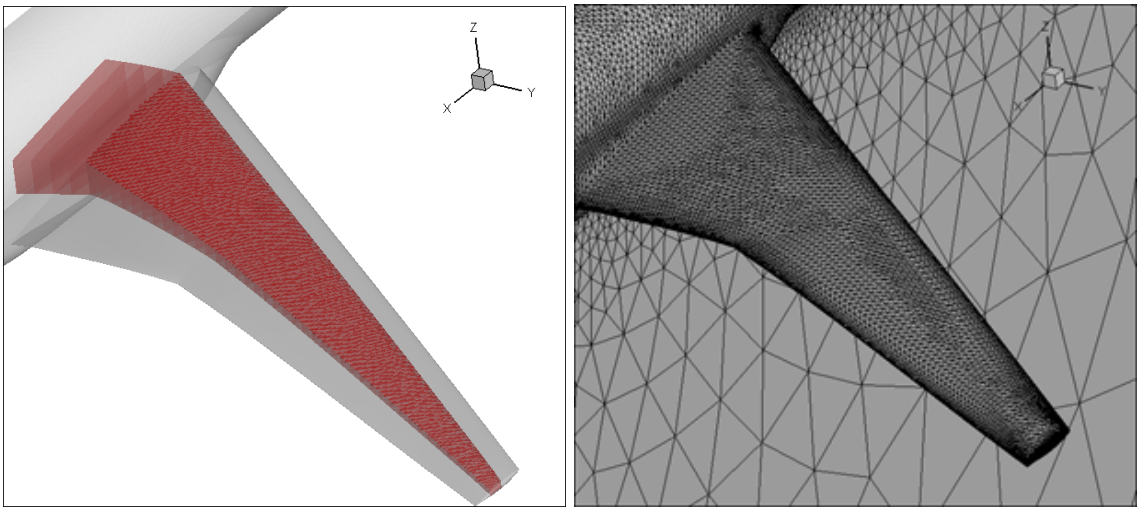

Figure 11. Structural finite element model of uCRM-9 wing-box visualized within outer mold line (left) and unstructured CFD grid on uCRM-9 wing surface (right).

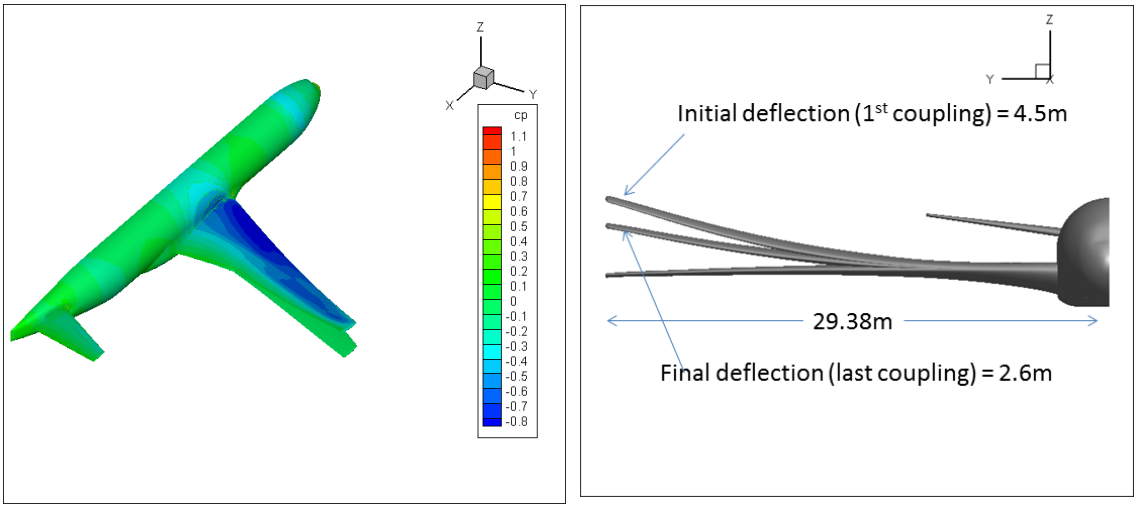

Figure 12. Aero-structural simulation results of uCRM-9 at cruise conditions ($M = 0.8$, $\alpha = 2°$, $Alt = 37,000ft$): Computed pressure distribution produced by NSU3D flow solver (left) and spanwise structural deflection at initial and final coupling fluid-structure coupling cycles (right).

aeroelastic deflection of the wing. At the first fluid-structure coupling cycle, the wing undergoes a large deflection, but then settles down to a tip deflection of 2.60 m as the coupled aero-structural system converges. This value is slightly higher than the tip deflection of 2.59m in reference,[27] and accordingly results in a slightly lower C_L value of 0.490 (at 2 degrees incidence) along with a drag coefficient of 0.0222, which is just under the reported value of 0.0226. These discrepancies may be due to modifications made to the structural model as discussed above, and/or due to the use of the coarse structural model and a relatively coarse CFD mesh. A grid refinement study is planned to further investigate the behavior of this test case using the current framework. However, the current results provide a baseline level of confidence in the accuracy of the current approach for the purposes of this work.

V. Aerostructural Analysis of Slotted Natural Laminar Flow Configuration

In this section, the aerostructural analysis capability is used to compute the flow over the notional SNLF aircraft configuration described previously in Section II. This test case requires the coupled solution of the flow (RANS) equations, a suitable transition model, along with the structural model response. In this case the one equation transition model of Mentor[17,18] coupled to the Spalart-Allmaras single equation turbulence model is used. As mentioned previously, although the structural model includes a wing strut, the effect of this component is not included in the aerodynamic model. The structural model used for this test case is described in Section II and

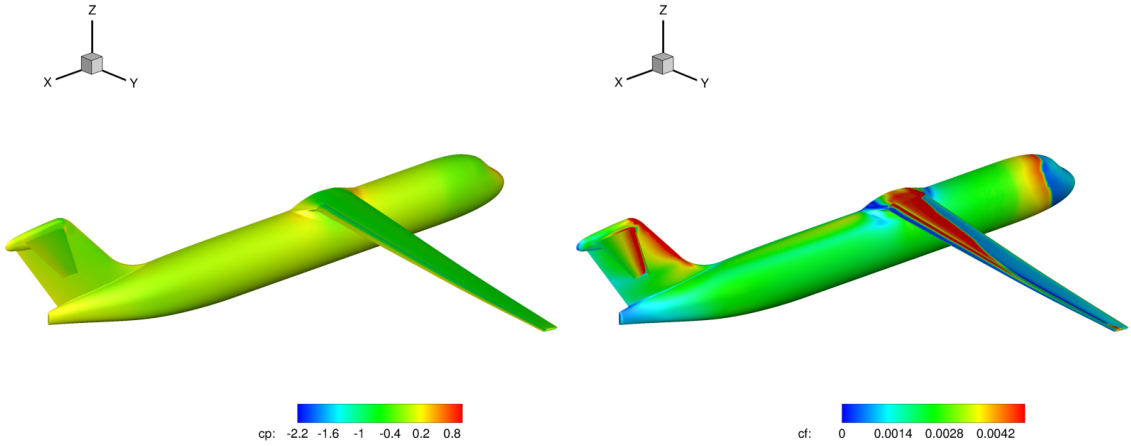

Figure 13. Computed surface pressure coefficient (left) and skin friction coefficient (right) over SNLF geometry for transitional aerostructural test case showing predicted laminar flow over main element of wing.

depicted in Figure 2. The unstructured CFD mesh contains approximately 9 million points and is illustrated in Figure 1. The flow conditions for this case are given as: $Mach = 0.5$, $\alpha = 1.7°$, $Re = 5 \times 10^6$. Figure 13 illustrates the solution computed for this test case (i.e. free transition with aerostructural deflections) in terms of computed surface pressure coefficients and skin friction coefficients. The computed skin friction distribution reveals that laminar flow is attained on the majority of the main element along the wing span, achieving the low drag design objective of this configuration. Figure 14 plots the convergence history of the force coefficients for the four different cases: free transition with aerostructural deflections, free transition with rigid geometry, and fully turbulent flow with and without aerostructural deflections. Additionally, the wing-tip deflection computed by these different scenarios is also shown in Figure 14. In general, relatively small deflections are observed inboard of the strut-wing attachment point, and the overall tip deflections are limited in magnitude due to the shorter span extent outboard of the strut attachment point. The computed aerodynamic forces for this case are given as $C_L = 0.485$ and $C_D = 0.0284$, for the case with free transition and aeroelastic deflections. For comparison, the corresponding values for this case without effect of structural deflections (i.e. rigid model) are $C_L = 0.495$ and $C_D = 0.0281$. The baseline case, using a rigid model and assuming fully turbulent flow produces values of $C_L = 0.431$ and $C_D = 0.0328$. The computed tip deflection for the full turbulent case is 10.54 inches, which increases to 13.49 inches for the free transition case (based on a wing half span of 1022 inches). These results illustrate the importance of including both transitional effects and structural effects in the analysis in order to obtain suitably accurate aerodynamic performance values.

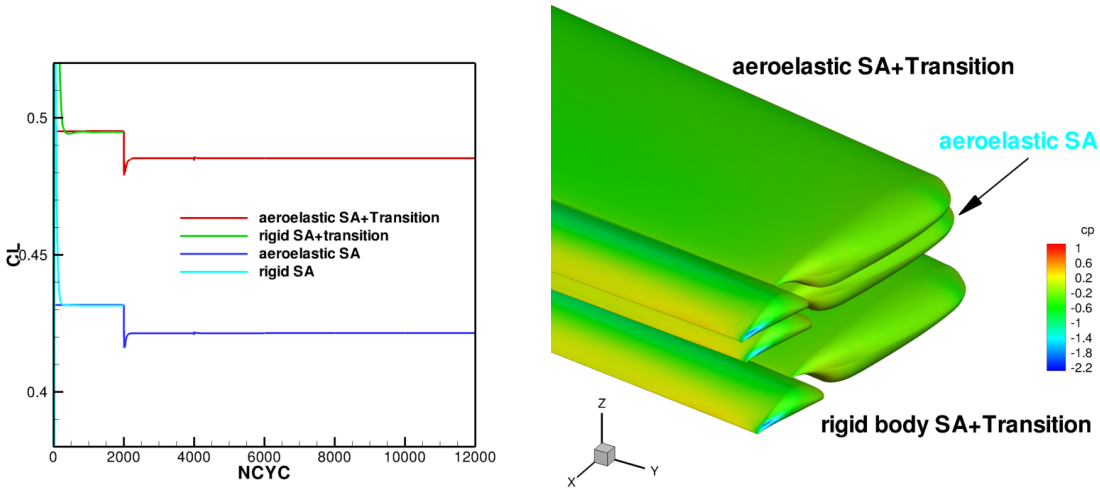

Figure 14. Convergence history of computed C_L for SNLF configuration showing variations in final steady state values obtained for cases with and without transition, as well as for rigid and coupled flexible structural model(left) and illustration of computed wing-tip deflection.

VI. Adjoint Sensitivities and Optimization

One of the principal objectives of this work is the development of a design optimization capability for SNLF aircraft configurations. As mentioned previously, a discrete adjoint formulation for computing sensitivities has been incorporated into all of the individual disciplinary components of the current analysis capability. However, at this stage we focus on the verification and demonstration of the adjoint-based optimization capability for natural laminar flow configurations in the absence of structural effects (i.e. rigid model). For this purpose we employ the notional SNLF aircraft configuration described previously with five design parameters defining wing twist at spanwise stations as shown in Figure 15.

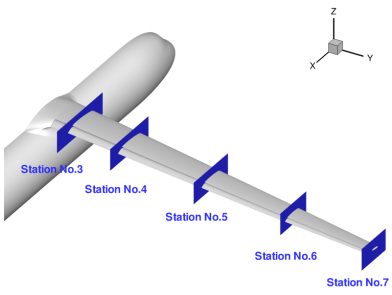

Figure 15. Illustration of spanwise stations for wing twist design variables.

An important consideration for the successful computation of sensitivities using the discrete adjoint approach is the ability to fully converge the primal equations prior to solving the adjoint system. As mentioned previously, the presence of the coupled transition equation(s) can significantly impair the ability of the solver to reach low residual or tolerance levels in convergence to steady state. In the current work, although a variety of transition models have been implemented

and validated, the single equation model of Mentor[17] coupled with the single turbulence equation of Spalart-Allmaras was found to offer the most robust strategy for achieving consistent convergence to steady state. However, even with this model, localized jumps in the intermittency values in the sublayer region may be observed which can stall convergence. Therefore, a strategy of freezing the intermittency values after a period of initial convergence during which the aerodynamic force coefficients achieve near constant values was adopted. Figure 16 illustrates the solution process for flow over the SNLF aircraft configuration at $Mach = 0.5$, $Re = 5 \times 10^6$ and an incidence of 1.76°. The convergence of the flow, turbulence and transition (intermittency) equations is shown in Figure 16(a), with the corresponding convergence in force coefficients given in Figure 16(b). As can be seen, convergence of the intermittency equations stalls out after approximately 500 cycles, which eventually leads to a slowdown or stalling of the turbulence and flow equations. However, the force coefficients achieve near constant values within this period of the convergence history. Therefore, the intermittency field is frozen after 750 cycles, after which convergence of the flow and turbulence equations resumes as the corresponding residuals are driven to machine zero over several thousand additional cycles.

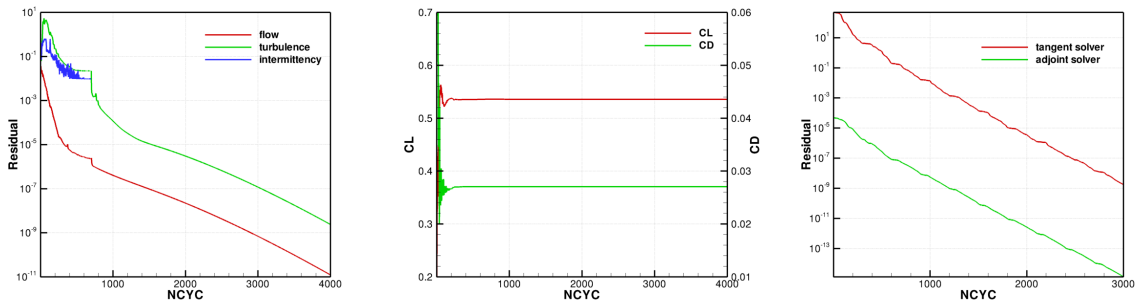

(a) (b) (c)

Figure 16. (a)Convergence history of flow, turbulence and transition(intermittency) equations;(b) Convergence history of computed force coefficients for initial configuration used in design optimization study; (c) Convergence history of tangent and adjoint solvers for computing sensitivities showing monotone convergence and similar convergence rates for both formulations.

Figure 16(c) depicts the convergence of the coupled system of discrete adjoint equations for the combined flow-turbulence-transition system linearized about the final state of the fully converged primal equations. The convergence of the tangent or forward linearization system is also shown. In both cases, the equations are solved using a restarted GMRES approach with line-implicit linear multigrid preconditioning, and monotone convergence to machine zero tolerance levels is observed with similar asymptotic convergence rates. Here the tangent system is used only for verification purposes and the similar convergence rates provide additional evidence that the adjoint system is solved appropriately, since theoretically these two linear problems contain the same eigenvalues and should converge at the same asymptotic rate. The adjoint-based sensitivities are verified by performing a duality check on the tangent and adjoint solutions. In this method, different random vector inputs are given to the tangent and adjoint solvers, and the inner product of the tangent input with the adjoint output should be equal to the inner product of the tangent output with the adjoint input vector. As shown in Table 1, agreement to 11 significant figures is obtained in the duality test.

In order to demonstrate the optimization process for flows with natural laminar transition, we construct a single objective function of the form:

Table 1. Summary of Dualcheck Results

Inner product of tangent dualcheck	-0.213050258944769E+04
Inner product of adjoint dualcheck	-0.213050258945033E+04

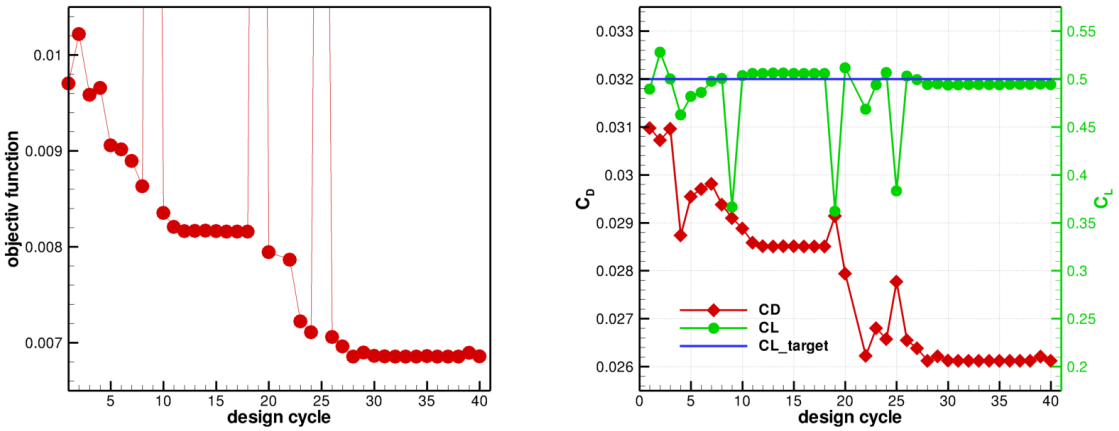

Figure 17. Convergence history for the objective function (left) and for integrated force coefficients CL and CD as a function of design cycles throughout the optimization process.

$$L = (C_L - C_{L_{Target}})^2 + 10(C_D - C_{D_{Target}})^2 \tag{3}$$

The adjoint-based sensitivities for this objective function with respect to the five wing twist design variables are computed at each design cycle and supplied to the SNOPT optimizer[29] which controls the overall optimization process. This objective formulation can be used to minimize drag at a prescribed or fixed lift condition. For these purposes, a target C_L value of 0.5 was chosen and the value $C_{D_{Target}} = 0.0$ was used to minimize drag in the optimization process. Although SNOPT is capable of performing constrained optimization, the above penalty-based objective formulation is used for simplicity at this stage.

For the initial configuration, we purposely apply an initial twist distribution that produces turbulent flow over a significant portion of the wing span, in order to investigate if the optimizer can find the low drag laminar flow solution. Figure 17 shows the optimization history of the objective and force coefficients over 40 design cycles. In this case the initial C_L and C_D values were 0.490 and 0.0310 respectively and and the optimization process resulted C_L and C_D values of 0.494 and 0.0261 respectively, corresponding to a drag reduction of 49 counts (at slightly higher lift). Figure 18 shows the computed skin friction coefficient on the initial and final optimized configuration, showing how the large regions of turbulent flow on the wing in the initial configuration have been replaced by laminar flow in the optimized configuration. Notably the region of laminar flow in the optimized configuration is even larger than that in the nominal configuration with no twist previously shown in Figure 13. The optimized wing twist includes approximately 0.5^o of negative twist at the wing tip, presumably in an effort to reduce induced drag.

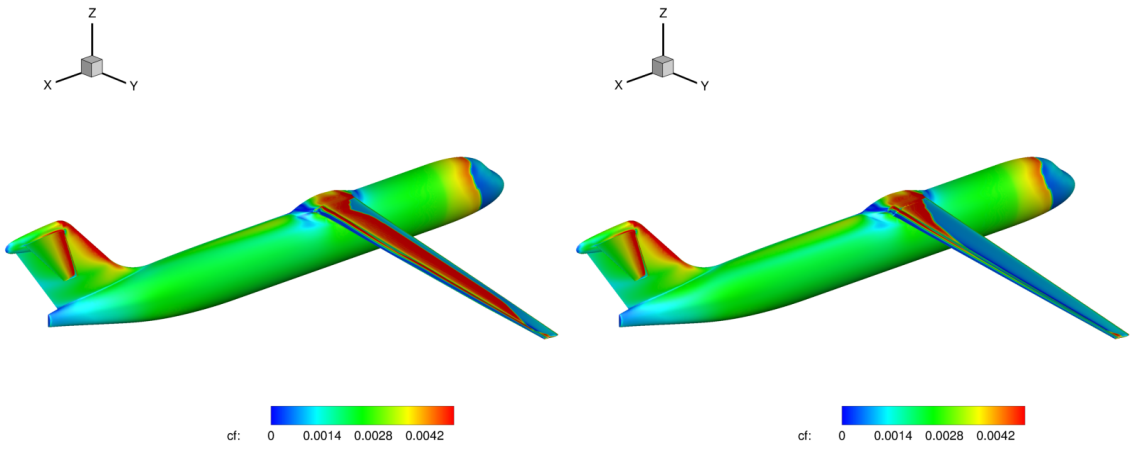

Figure 18. Computed skin friction distribution for initial configuration (left) and optimized configuration (right) for wing twist optimization run.

VII. Conclusion

This paper describes a comprehensive multidisciplinary analysis and design strategy and its application to slotted natural laminar flow(SNLF) aircraft configurations. The use of unstructured meshes facilitates the treatment of slotted wing configurations, while the incorporation of a suitable transition model is essential for capturing the physics that enable the superior performance of these designs. Additionally, the ability to incorporate the effects of structural deformations takes on increased importance for high aspect ratio wings typical of these configurations. The feasibility of performing adjoint-based design optimization for SNLF configurations using the current approach was also demonstrated in this work. Additional efforts are underway to demonstrate the complete SNLF aerostructural optimization capability. At the same time, challenges persist in the ability to consistently converge natural laminar flow problems on complex geometries, primarily due to the non-smooth behavior of the intermittency field produced by current transition models. Although this deficiency can be often overlooked for analysis problems, this issue takes on additional importance for adjoint-based design optimization problems where convergence to tight tolerances of all equations is required in order to obtain accurate sensitivities. Future work will also investigate approaches for resolving this behavior of the intermittency field in current transition models.

VIII. Acknowledgments

This material is based upon work supported by the National Aeronautics and Space Administration (NASA) under cooperative agreement award number NNX17AJ95A. The work was performed under the University Leadership Initiative (ULI) at the University of Wyoming as a subcontract to the University of Tennessee, Knoxville "Advanced Aerodynamic Design Center for Ultra-Efficient Commercial Vehicles." Computer time was provided by the University of Wyoming Advanced Research Computing Center (ARCC) and by the NCAR-Wyoming Supercomputer Alliance.

References

[1]M. D. Maughmer. Benefits of using a slotted, natural-laminar-flow airfoil to business-jet, cruise performance. Airfoils, Inc, July, 2004.

[2]D. M. Somers and M. D. Maughmer. Design and experimental results for the S414 airfoil. U.S. Army Research, Development and Engineering Command, RDECOM TR 10D-112, August, 2010.

[3]Dan M. Somers. Design of a slotted, natural-laminar-flow airfoil for business-jet applications. NASA/CR-2012-217559, July, 2012.

[4]J. G. Coder, M. D. Maughmer, and D. M. Somers. Theoretical and experimental results for the S414, slotted, natural-laminar-flow airfoil. *Journal of Aircraft*, 51(6):1883–1890, 2014.

[5]M. D. Maughmer, A. Premi, and D. M. Somers. Exploration of a Slotted Laminar-Flow-Control airfoil concept. Final Technical Report, NASA Grant No. NNX13AB86A, Nov., 2013.

[6]D. W. Levy, K. R. Laflin, J. C. Vassberg, E. Tinoco, M. Mani, B. Rider, O. Brodersen, S. Crippa, C. L. Rumsey, R. A. Wahls, J. Morrison, D. J. Mavriplis, and M. Murayama. Summary of data from the fifth aiaa cfd drag prediction workshop. AIAA Paper 2013-046, presented at the 51st Aerospace Sciences Meeting, Grapevine TX, January 2013.

[7]D. M. Somers. An exploratory investigation of a slotted, natural-laminar-flow airfoil. NASA/CR-2012-217560, April, 2012.

[8]M. K. Bradley and C. K. Droney. Subsonic ultra green aircraft research: Phase I final report. Boeing Research and Technology, Huntington Beach, California, NASA/CR2011-216847, 2011.

[9]D. J. Mavriplis and K. Mani. Unstructured mesh solution techniques using the NSU3D solver. AIAA Paper 2014-081, 52nd Aerospace Sciences Meeting, National Harbor, MD, January 2014.

[10]S. R. Allmaras, F. T. Johnson, and P. R. Spalart. Modifications and clarifications for the implementation of the spalart-allmaras turbulence model. ICCFD7-1902, 7th International Conference on Computational Fluid Dynamics, Big Island, Hawaii, 9-13 July, 2012.

[11]D. J. Mavriplis and V. Venkatakrishnan. A unified multigrid solver for the Navier-Stokes equations on mixed element meshes. *International Journal of Computational Fluid Dynamics*, (8):247–263, 1997.

[12]D. J. Mavriplis, M. Long, T. Lake, and M. Langlois. NSU3D results for the second AIAA high-lift prediction workshop. AIAA Paper 2014-748 52nd Aerospace Sciences Meeting, National Harbor, MD., 2014.

[13]M. Park, K. R. Laflin, M. Chaffin, N. Powell, and D. W. Levy. CFL3D, FUN3D and NSU3D contributions to the fifth drag prediction workshop. AIAA Paper 2013-0050, 51st AIAA Aerospace Sciences Meeting, Grapevine TX, January 2013.

[14]D. J. Mavriplis. Discrete adjoint-based approach for optimization problems on three-dimensional unstructured meshes. *AIAA Journal*, 45(4), 2007.

[15]R. B. Langtry and F. R. Menter. Correlation-based transition modeling for unstructured parallelized computational fluid dynamics codes. *AIAA Journal*, 47(12):2984–2906, 2009.

[16]J. G. Coder, T. H. Pulliam, and J. C. Jensen. Contributions to HiLiftPW-3 using structured, overset grid methods. AIAA Paper 2018-1039, AIAA SciTech Forum, January, 2018.

[17]F. R. Menter, P. E. Smirnov, T. Liu, and R. Avancha. A one-equation local correlation-based transition model. *Flow, Turbulence and Combustion*, 95(4):583–619, 2015.

[18]R. H. Nichols. Addition of a local correlation-based boundary layer transition model to the createtm-av kestrel unstructured flow solver. AIAA SciTech Forum, 2019-1343, January, San Diego, California, 2019.

[19]E. Anderson. Development of an adjoint-based structural optimization capability. PhD Thesis, University of Wyoming, December 2019.

[20]D. Mavriplis, E. Anderson, R. Fertig, and M. Garnich. Development of a high-fidelity time-dependent aero-structural capability for analysis and design. AIAA Paper 2016-1175, 54th AIAA Aerospace Sciences Meeting, San Diego CA, January 2016.

[21]S. W. Sloan. A FORTRAN program for profile and wavefront reduction. *International Journal for Numerical Methods in Engineering*, 28(11):2651–2679, 1989.

[22]P. R. Amestoy, I. S. Duff, J.-Y. L'Excellent, and J. Koster. MUMPS: a general purpose distributed memory sparse solver. In *Applied Parallel Computing. New Paradigms for HPC in Industry and Academia*, pages 121–130. Springer, 2001.

[23]B. M. Kulfan. Universal parametric geometry representation method – "CST". AIAA-Paper 2007-0062, 45th AIAA Aerospace Sciences Meeting and Exhibit, January 2007.

[24]Z. Yang and D. J. Mavriplis. A mesh deformation strategy optimized by the adjoint method on unstructured meshes. *AIAA Journal*, 45(12):2885–2896, 2007.

[25]R. Petzold and R. Radespiel. Transition on a wing with spanwise varying crossflow and linear stability analysis. *AIAA Journal*, 53(2):321–325, 2015.

[26]J. G. Coder. Further development of the amplification factor transport transition model for aerodynamic flows. AIAA Paper 2019-0039, AIAA SciTech Forum, January, 2019.

[27]T.R. Brooks, G.L.W. Kenway, and J.R.R.A. Martins. Benchmark aerostructural models for the study of transonic aircraft wings. *AIAA Journal*, 56(7):2840–2855, 2018.

[28]G. K. W. Kenway G. J. Kennedy and J. R. R. A. Martins. High aspect ratio wing design: Optimal aerostructural tradeffs for the next generation of materials. Proceedings of the AIAA Science and Technology Forum and Exposition (SciTech), National Harbor, MD, January, 2014.

[29]P. E. Gill, W. Murray, and M. A. Saunders. SNOPT: An SQP algorithm for large-scale constrained optimization. *SIAM journal on optimization*, 12(4):979–1006, 2002.